Annealing Optimization for HZO Thin Films with In-Situ STEM EBIC Characterization

Yueyun Chen, Ho Leung Chan, Tristan P O'Neill, Megan K Lenox, William A Hubbard, Jon F Ihlefeld, B C Regan

Microscopy and Microanalysis, **31** (7), 2025, 1098–1101
https://doi.org/10.1093/mam/ozaf048.574

Microscopy AND Microanalysis

Proceedings

Annealing Optimization for HZO Thin Films with *In-Situ* STEM EBIC Characterization

Yueyun Chen[1,2], Ho Leung Chan[1,2], Tristan P. O'Neill[1,2], Megan K. Lenox[3], William A. Hubbard[4], Jon F. Ihlefeld[3,5], and B. C. Regan[1,2,4,*]

[1]*Department of Physics and Astronomy, University of California, Los Angeles, CA, U.S.A.*
[2]*California NanoSystems Institute (CNSI), University of California, Los Angeles, CA, U.S.A.*
[3]*Department of Material Science and Engineering, University of Virginia, Charlottesville, VA, U.S.A.*
[4]*NanoElectronic Imaging, Inc., Los Angeles, CA, U.S.A.*
[5]*Charles L. Brown Department of Electrical and Computer Engineering, University of Virginia, Charlottesville, VA, U.S.A.*
*Corresponding author: regan@physics.ucla.edu

Hafnium zirconium oxide (HZO), a ternary oxide exhibiting ferroelectric properties, has gathered significant attention in recent years due to its potential for integration into the next generation computer memory. However, its ferroelectric phase (orthorhombic, o-phase) is metastable and difficult to stabilize in thin film [1, 2]. To optimize the device functionality, maximizing the o-phase through a controlled annealing process while keeping the leakage current low is critical [3]. Conventional rapid thermal annealing (RTA) techniques lack the capability to monitor the structural and functional evolution in real time, which hinders the optimization of device performance and longevity. This study addresses the gap by annealing functional HZO capacitors in a scanning transmission electron microscope (STEM) while monitoring both their crystal structure and their ferroelectric performance using electron beam induced current (EBIC) imaging [4].

The devices are fabricated on a silicon substrate. Each comprises a 3 μm × 3 μm HZO capacitor surrounded by an on-chip resistive heater (Fig. 1A). The capacitor is a vertical stack consisting of a 20 nm titanium nitride (TiN) bottom electrode, a 10 nm HZO layer, and a 10 nm TiN top electrode (Fig. 1B). The on-chip heater is a 20 nm thick TiN wire, enabling *in-situ* thermal control.

Starting with a pristine (amorphous) HZO capacitor, the experiment is conducted as follows. After annealing the sample with predefined heater power and duration, we characterize the device's ferroelectric response with the positive-up-negative-down (PUND) technique before and after 10^4 field cycles [5]. We acquire STEM (both standard and EBIC) images of the sample in both polarization states. Then we repeat the process with a longer annealing time or higher heater power. All imaging and PUND measurements are performed at room temperature.

Annular dark field (ADF) images acquired simultaneously with EBIC (Fig. 2A) reveal the progressive crystallization of the HZO film. The crystalline phase first appears near the TiN heater and propagates towards the capacitor as heater power increases. To estimate the sample temperature as a function of heater power, we assume $\Delta T \propto P$ and that the crystallization temperature of HZO is 350 °C [6].

Before the HZO in the capacitor crystallizes, EBIC measures negligible electric fields in the sample. Afterward, EBIC imaging visualizes the significant ferroelectric depolarization fields. The switching area initially grows with an increasing annealing temperature (Fig. 2B, C). The EBIC imaging measurements are consistent with the increase in remanent polarization (P_r) derived from the PUND transport measurements (Fig. 2D, E). Annealing at temperatures above the crystallization temperature further enhances the ferroelectric response of the HZO, up to a point. With further increase in the annealing temperature the ferroelectric response eventually ceases improving and the device leakage current starts to grow.

Maps of the remanent switching field (E_{rs}) and remanent background field (E_{rb}) are derived from EBIC images [4]. E_{rs} highlights the switching domains, while E_{rb} highlights pinned domains or any asymmetric ferroelectric response. High-resolution E_{rs} maps acquired at the top-left corner of the capacitor reveal ferroelectric domains with dimensions of ~10 nm (Fig. 3C). As the annealing temperature increases, more domains show up, consistent with the lower-resolution results (Fig. 2). Pinned domains become visible after the device is annealed at 400 °C (Fig. 3B, C red circles). These domains are missing from the E_{rs} map and possess a positive E_{rb}, which means they are polar but pinned in the polarized down state. Maps post 510 °C annealing show that these domains become switchable and no longer have significant E_{rb} compared to the surroundings. Thus high temperature annealing can lead to depinning and corresponding increases in P_r and the switching fraction.

While ADF images can effectively discriminate between crystal structures with distinct Bragg angles (for example, HZO and TiN in Fig. 2A and Fig. 3A), it lacks the sensitivity to resolve subtle phase differences. 4D STEM acquires a convergent beam electron diffraction (CBED) pattern at each beam position and generates a spatially resolved diffraction dataset. These CBED patterns are information-rich and can be used to retrieve phase information [7]. Fig. 4 illustrates a preliminary 4D STEM dataset acquired on a HZO capacitor with carbon electrodes. The Bragg disks are localized using py4DSTEM, and a Bragg peak map is synthesized by integrating localized Bragg disk across the scan area (Fig. 4B) [8]. Several diffraction rings corresponding to the o-phase (ferroelectric), m-phase (non-FE monoclinic phase), and t-phase (non-FE tetragonal phase) of HZO are identified. By correlating these diffraction signatures with individual CBED patterns, the phase distribution and phase fraction can be quantified [9].

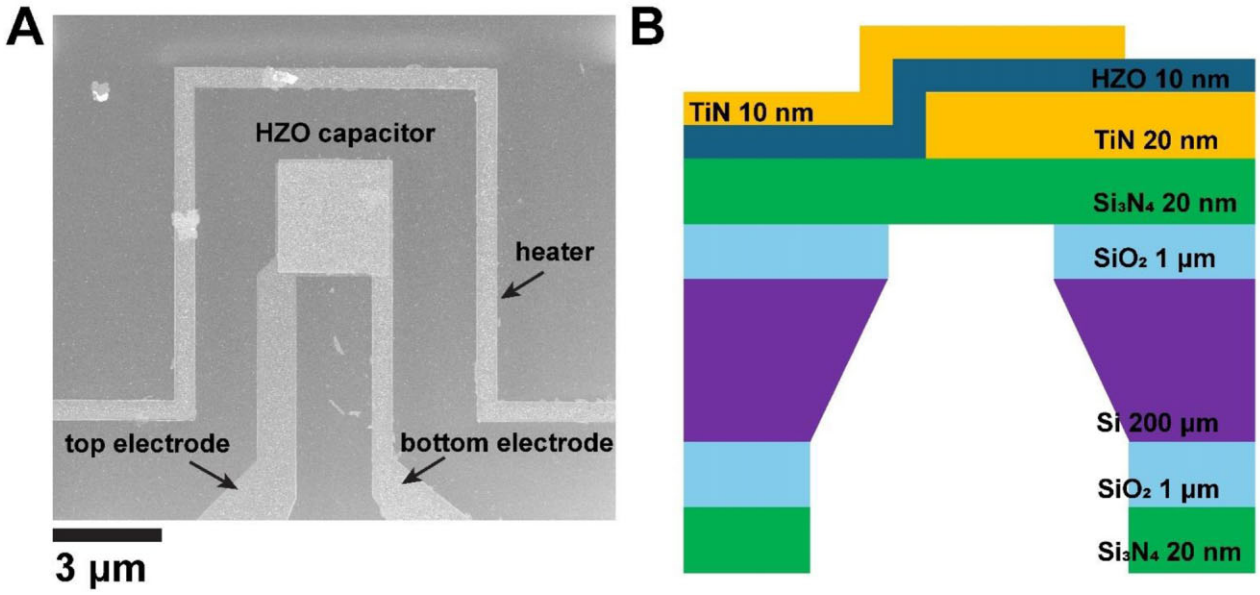

Fig. 1. A) ADF image of the ferroelectric capacitor and the on-chip heater. B) A schematic diagram of the cross-section view of the capacitor fabricated on the Si substrate. The electron transparent window is 30 μm wide.

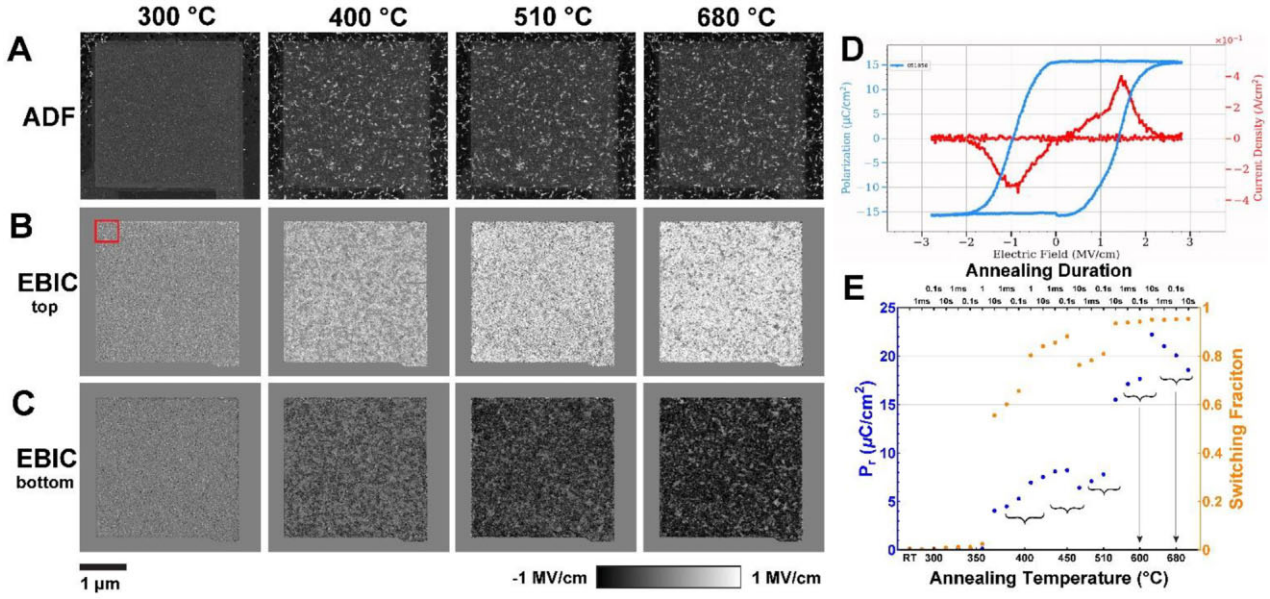

Fig. 2. STEM/EBIC images of the HZO capacitor after 10 s annealing at different temperatures. A) ADF images of the capacitor before and after HZO crystallization. B, C) EBIC images collected from top and bottom electrodes with the capacitor in the polarized down state. Positive electric field represents a field pointing towards the electrode. The red box in B) highlights the region where Fig. 3 data is acquired. D) A hysteresis loop derived from PUND measurement after the device is annealed at 510 °C for 10 s. E) P_r measured with PUND and switching fraction measured with EBIC show consistent trends as the annealing temperature/duration goes up. The degradation in ferroelectric response between 450 and 510 °C annealing is a result of excessive electron dose from a calibration procedure, which is healed after annealing at a higher temperature.

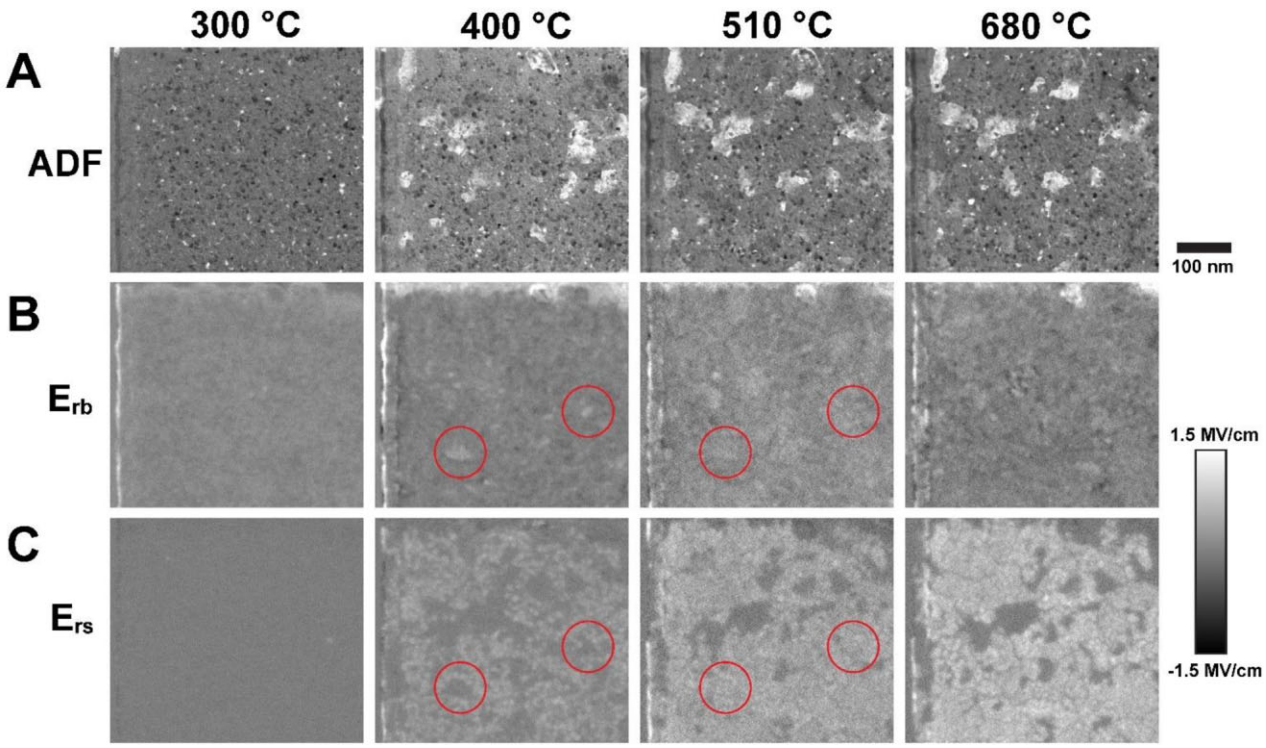

Fig. 3. Internal fields of the top left corner of the capacitor derived from STEM EBIC after 10 s annealing at different temperatures. A) HZO grains appear after 400 °C. B) The remanent background field, which highlights pinned domains. C) The remanent switching field, which highlights switching domains. Red circles indicate two domains that are pinned at 400 °C but unpin after heating at 510 °C. Heating at elevated temperatures can thus lead to domain depinning.

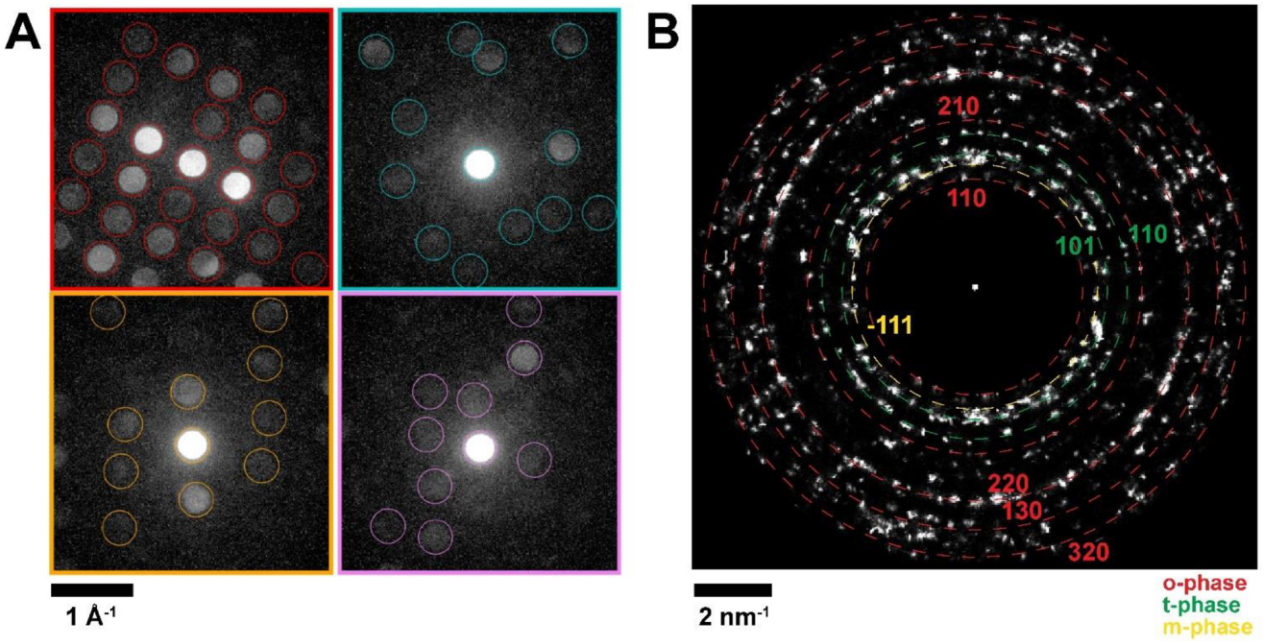

Fig. 4. A) 4D-STEM diffraction patterns acquired on a HZO capacitor with carbon electrodes. Bragg disks are detected and localized using py4DSTEM. B) Bragg peak map accumulated over the scan area, diffraction rings from distinct HZO phases are identified.

References

1. Siannas N *et al. Commun Phys* (2022) **5**, 178. https://doi.org/10.1038/s42005-022-00951-x
2. Shi S *et al. Nat Commun* (2023) **14**, 1780. https://doi.org/10.1038/s41467-023-37560-3
3. Kim Y *et al. Current Applied Physics* (2020) **20**, 1441–1446. https://doi.org/10.1016/j.cap.2020.09.013

4. Chan HL *et al. ACS Nano* (2024) **18**, 20380–20388. https://doi.org/10.1021/acsnano.4c04526
5. Martin S *et al. Rev. Sci. Instrum.* (2017) **88**, 023901. https://doi.org/10.1063/1.4974953
6. Jung YC *et al. Appl. Phys. Lett.* (2022) **121**, 222901. https://doi.org/10.1063/5.0126695
7. Folastre N *et al. Sci Rep* (2024) **14**, 12385. https://doi.org/10.1038/s41598-024-63060-5
8. Savitzky BH *et al. Microscopy and Microanalysis* (2021) **27**, 712–743. https://doi.org/10.1017/S1431927621000477
9. The data was acquired at the Electron Imaging Center for Nanomachines (EICN) at the University of California, Los Angeles's California for NanoSystems Institute (CNSI). This work is supported by the National Science Foundation (NSF) Science and Technology Center (STC) award DMR-1548924 (STROBE). Thin film growth was supported by the Semiconductor Research Corporation (SRC) via task 2875.001 within the Global Research Collaboration program.